An anatomically realistic temperature phantom for radiofrequency heating measurements

Nadine N. Graedel[1], **Jonathan R. Polimeni**[1,2], **Bastien Guerin**[1], **Borjan Gagoski**[3], and **Lawrence L. Wald**[1,2,4]

[1] A. A. Martinos Center for Biomedical Imaging, MGH, Charlestown, MA, United States

[2] Harvard Medical School, Boston, MA, United States

[3] Department of Electrical Engineering and Computer Science, Massachusetts Institute of Technology, Cambridge, MA, United States

[4] Harvard-MIT Division of Health Sciences and Technology, MA, Cambridge, United States

Abstract

Purpose—An anthropomorphic phantom with realistic electrical properties allows for a more accurate reproduction of tissue current patterns during excitation. A temperature map can then probe the worst-case heating expected in the un-perfused case. We describe an anatomically realistic human head phantom that allows rapid 3D temperature mapping at 7 T.

Methods—The phantom was based on hand-labeled anatomical imaging data and consists of four compartments matching the corresponding human tissues in geometry and electrical properties. The increases in temperature resulting from radiofrequency excitation were measured with MR thermometry using a temperature sensitive contrast agent ($TmDOTMA^{-}$) validated by direct fiber optic temperature measurements.

Results—Acquisition of 3D temperature maps of the full phantom with a temperature accuracy better than 0.1°C was achieved with an isotropic resolution of 5 mm and acquisition times of 2–4 minutes.

Conclusion—Our results demonstrate the feasibility of constructing anatomically realistic phantoms with complex geometries incorporating the ability to measure accurate temperature maps in the phantom. The anthropomorphic temperature phantom is expected to provide a useful tool for the evaluation of the heating effects of both conventional and parallel transmit pulses and help validate electromagnetic and temperature simulations.

Keywords

phantom; thermometry; MR safety; local SAR; parallel transmit; temperature estimation

Correspondence address Prof. Lawrence L. Wald Building 75, Room 2.109 Charlestown, MA 02129 USA wald@nmr.mgh.harvard.edu Tel: 617-724-9706 Fax: 617-726-7422.

Introduction

Quantifying the heating induced by absorption of the radiofrequency (RF) energy used for excitation in magnetic resonance imaging is a major focus in MR safety. Because the human body is not a uniform conductor but contains many different tissue types with different geometrical and electrical properties, the RF current paths are shaped by the geometry of the conductive tissue. Thus the heating pattern in the body is complicated and focal local maxima in Specific Absorption Rate (SAR) and heating can occur. Because SAR, and temperature, are constrained by the distribution of high-conductivity tissues, a slight variation in geometry can have large effects on the distribution of heating (1,2). While this holds even at lower fields (e.g. 1.5 T) the situation becomes even more complicated at high and ultra-high field where wavelength effects enter and may exacerbate the problem by increasing the spatial complexity of the heating pattern. The primary concern is the formation of localized heating (“hotspots”) where cells can be significantly damaged even if the global SAR is within the limits.

The issue of local hotspots and the need to validate the electromagnetic models used to predict them has become more relevant over the last years with the development of parallel transmission (pTx) (3). In pTx excitations, several RF coils are used, each playing a distinct RF pulse (3,4). This allows the inherent spatial independence across the elements of the array to be exploited. The magnitude and phase of the transverse magnetization produced by each channel can thus be tailored to mitigate the B_1^+ inhomogeneity (5-7), which is an impediment to routine clinical scanning at high fields. Using the additional degrees of freedom provided by a pTx coil, accelerated 2D and 3D spatially selective RF excitations can be designed that are significantly shorter than if they were designed on a single channel system. In pTx, the local electric fields generated by each coil element also undergo superposition during transmit and thus local extrema of electric field magnitude can occur. Additionally, the electric fields in the tissue are shaped by the geometry of conducting structures. Together, these effects can create local SAR hotspots, characterized by a large ratio of local SAR to global SAR (8). SAR hotspots, and the associated local temperature increase and risk of tissue damage, are a major concern in pTx and one of the main obstacles preventing the introduction of this technology into routine clinical use.

Most MRI scanners ensure patient safety by measuring and limiting the power entering the transmit coil (forward minus reflected power) and assuming that 100% of this power is deposited in the body mass immersed in the RF field. This procedure is complicated in a transmit array where element-to-element interferences are critical and must be taken into account. When pTx is used, both the global and local SAR are not only dependent on the pulse waveforms sent to the different channels but also on the time-varying constructive and destructive interferences between the array elements. Even the monotonic relationship between applied power and SAR can be disrupted (9). For example, local SAR may increase even if the power to a given channel is decreased if that channel was destructively interfering with the electric fields from the other channels. For these reasons, it is challenging to predict based solely on the applied power level whether local SAR hotspots arise from a given set of pulse waveforms. SAR must therefore be computed for every set of pulses. It is important to note that the electric field, which is relevant for determining the

SAR pattern, and magnetic field produced by a coil element do not correspond. Therefore one cannot directly assess SAR or temperature hot spots by B_1 field mapping.

The SAR hotspots can be assessed by simulation of the field superposition of the array elements in a human body model (10). Because temperature change, rather than SAR, is the direct physical agent of the damage done to tissues, a subsequent temperature simulation should also be performed (11). Electromagnetic and thermodynamic simulations are important tools to evaluate the safety of MR protocols, and are critical in pTx (12).

The ability to complement SAR modeling with temperature measurements in phantoms has become an important part of validating MR transmit safety, for example around implanted objects (ASTM Standard F2182–11a). Ideally, however, it would be possible to evaluate the heating pattern in vivo. A number of MR thermometry methods exist (11), of which MR thermometry based on the temperature dependence of the proton resonance frequency of water (12) is the most common. However, the difficulty of mapping the small (<1°C) temperature changes relevant to MR transmit safety has limited its use in vivo temperature mapping to a few studies (13,14). Most of the in vivo temperature mapping work has concentrated on monitoring the larger, intentional heating in RF ablation (15,16), focused ultrasound (17) or hyperthermia (18).

While studies using animal models, for example recent studies on the effect of RF exposure in swine (19), have provided useful information, translation of this knowledge to human imaging is confounded by the differing dielectric geometry from the human head. Furthermore, anesthesia has been shown to have a large effect on thermoregulation (20,21) complicating comparison to non-anesthetized human studies. Therefore the use of animal studies alone, without supporting information from other measurements, has been questioned (22). For these reasons we propose the use of an anthropomorphic phantom to more accurately mimic the geometry of the high-dielectric components in the human head as a useful tool for supplementing other MR safety tests and as a validation tool for electromagnetic and temperature simulations.

In this study, we designed and fabricated a realistic human head phantom from anatomical-labeled MRI data consisting of three tissue compartments filled with gel doped to have biologically accurate dielectric properties and the low-conductivity areas (bone and air) printed in plastic. We measured temperature in this phantom using MR thermometry at 7 T, and validated temperature imaging measurements with inserted temperature probes. To increase the speed and accuracy of the temperature measurements we used a temperature sensitive contrast agent: thulium 1,4,7,10- tetraazacyclododecane-1,4,7,10-tetramethyl-1,4,7,10-tetraacetic acid ($TmDOTMA^-$) (23). We demonstrate an accuracy better than 0.1 °C for temperature imaging with this phantom in less than 3 minutes and with a resolution better than 5 mm isotropic, suggesting that temperature imaging with an anatomically accurate phantom can provide a sensitive tool for evaluating the spatial patterns of temperature increases.

Methods

Phantom design

The model of the human head was generated from 1 mm isotropic T_1-weighted MR image volumes of a human head manually labeled into 30 tissue types (Fig. 1a) by a trained neuroanatomist at the Center for Morphometric Analysis at the Massachusetts General Hospital (24). From this labeled tissue data, four compartments were extracted: brain (consisting of gray matter, white matter, and both ventricular and peripheral cerebrospinal fluid); muscle (consisting of the tissue classes muscle and subcutaneous fat/muscle); eye (consisting of cornea, sclera, lens, vitreous humor, and aqueous humor); and the remaining tissue classes including the skull, which were lumped into a single enclosing compartment. Using the simplifying assumption that most of these remaining tissue types are low dielectric constant tissues (such as bone, air and fat) we term this compartment the low dielectric constant compartment.

To generate a CAD model from this tissue data, surface mesh representations of the boundaries of the four volumes were generated separately (using the marching cubes algorithm implemented in the FreeSurfer program “mri_tessellate”, then Laplacian smoothing with Freesurfer tool “mris_smooth”). In this step minor manual edits were made in order to make the phantom model compatible with fabrication, such as ensuring a minimum thickness to the tissues to prevent the surface meshes of the different tissues from intersecting.

Filling tubes were added to the CAD model to allow the muscle and brain cavities to be filled from an external source and additional modifications were made to the openings of the channels to allow mechanical caps to seal the filled phantom. A small hole was also added to each eyeball near the pupil to allow for filling and, which could be sealed with epoxy. Two ports of 2 mm diameter where created to allow the insertion of fluorescent fiber optic temperature probes into the brain compartment. The final phantom model (see Fig. 1) had a bounding box sized 17×22×25 cm^3 and the total volume of all the cavities (brain, muscle and eye compartments) was 3.1 L. The CAD model of the phantom with and without filling channels can be downloaded on http://phantoms.martinos.org

Phantom fabrication

The low conductivity compartment comprising the main structure of the phantom was 3D printed in a composite of polycarbonate (PC) and acrylonitrile butadiene styrene (ABS) plastic in two pieces. The printing was performed by a rapid prototyping service (RedEye on Demand, Eden Prairie, MN USA), which uses Stratasys/Fortus 3D printers. Printing in two pieces was required to allow for complete removal of the temporary support material used in 3D printing. In this case, the support material is dissolved in a caustic bath, and printing the part in two halves facilitated the access of the chemical solution to the interior cavities of the phantom. The anthropomorphic phantom was treated with a sealant to render the printed plastic watertight using the manufacturer's proprietary method. (For our prototype polycarbonate printed phantoms, we have used an acetone dip or an epoxy dip for simple

phantom shapes, and the processes performed similarly to the manufacturer's proprietary method.)

The three high conductivity compartments comprising the phantom cavities were filled with tissue-mimicking material. Since a liquid phantom is not appropriate for temperature measurements due to the effect of convection, which leads to significant underestimation of temperature increases (25), we chose an agar gel material that could be injected into the phantom through the fill channels. After cooling the agar gels produce the desired low-convection material. Each of the three tissue compartments was filled with a specific gel mixed to mimic the dielectric properties of the corresponding tissue type. I.e. the relative permittivity (ε_r) and conductivity (σ) of the gels were matched to those of human brain, muscle and eye tissue. Following the suggestion of Ito et al. (26) the permittivity was decreased by adding polyethylene powder (ultra-high molecular weight, Sigma-Aldrich, St. Louis, MO, USA) and the conductivity was increased by adding salt. Sodium Azide (NaN_3) was added as a preservative (see Table 1 for list of mixtures). Approximately 2 mM of $TmDOTMA^-$ was added to each gel mixture. The $TmDOTMA^-$ was synthesized from $DOTMA^{4-}$ (Macrocyclics, Dallas, TX, USA) and thulium chloride. The desired dielectric properties were taken from the parametric model by Gabriel et al. (27) for a frequency of 297 MHz. The target values for the muscle compartment are σ = 0.77 S/m and ε_r = 58. For the brain compartment a weighted average of 1.3 (28) between white and gray matter was used based on the ratio of their volumes in the human brain, which results in the target values of σ = 0.57 S/m and ε_r = 51 for the brain phantom tissue. For the eyes the dielectric properties of vitreous humor were used: σ = 1.52 S/m and ε_r = 69.

To confirm the dielectric properties of the gels, the properties were measured using a dielectric probe (AT-85070E dielectric probe kit, Agilent Technologies, Palo Alto, CA, USA). For each gel and electrical property, we repeated the measurement 40 times resulting in the following values for brain, ε_r=50.8±0.7 σ=0.63±0.01 S/m; for muscle ε_r=58.7±0.9 σ= 0.72±0.01 S/m; and for the eye tissue ε_r=68.6±0.7 σ=1.65±0.03 S/m. The measured permittivity is in very good agreement (differences smaller that 1.5%) with the target values, and the conductivity values did not deviate more than 10.5% from the target values.

Temperature imaging

Temperature imaging was performed on a 7T human whole-body scanner (Siemens Healthcare, Erlangen, Germany). Temperature maps were generated through a conventional temperature imaging approach based on calculating the phase difference between a pair of gradient-recalled echo (GRE) images. For GRE acquisitions, the MR image phase change $\Delta\phi$ due to a temperature change ΔT is given by

$$\Delta T = \Delta\varphi / (2\pi \quad \gamma \quad B_0 \quad c \quad TE), \quad [1]$$

where B_0 is the amplitude of the static field, γ is the gyromagnetic ratio, TE is the echo time of the image acquisition, and c is a temperature coefficient in units of ppm/°C (29,30). $TmDOTMA^-$ has a temperature coefficient of c = 0.6 ppm/°C (23), which is 60 times greater than that of water (c = −0.01 ppm/°C) and of the opposite sign. We selectively excited the methyl resonance of the $TmDOTMA^-$ at −106 ppm, which at 7 T corresponds to

a −31.5 kHz shift from the water resonance (see Fig. 2a). This methyl resonance consists of 12 magnetically equivalent protons on four methyl groups. We did not measure the T_1 and T_2 of this resonance at 7 T but it has been reported as T_1 = 5.3 ms and T_2 = 4.1 ms at 9.4 T (23). All temperature imaging protocols utilized a 2.56 ms sinc RF excitation pulse with a time-bandwidth product of 10, which was shifted −31.5 kHz off water resonance, achieved by manually adjusting the scanner center frequency. This narrow-width pulse was capable of adequately avoiding excitation of the water protons, and therefore eliminated water signal from the $TmDOTMA^-$ images. Residual water signal is shifted 31.5 kHz in the frequency encoding direction and therefore lies outside or towards the edge of the field of view, see Fig. 2a.

Because of the large temperature coefficient of $TmDOTMA^-$, large phase shifts can be introduced by even moderate temperature changes. Therefore the readout bandwidth was chosen to be high enough to prevent translation of the image as the temperature changed. However, because higher bandwidths also result in lower image SNR, we chose an intermediately high bandwidth near 75 kHz across the image (exact bandwidths are reported for individual experiments). For a bandwidth of 75 kHz, a temperature increase of approximately 10 °C results in a one-pixel shift in the readout direction. Since in our experiments temperature changes were lower than 10 °C, we ignored this sub-pixel shift.

During the acquisition, the temperature was simultaneously measured by fiber optic fluorescence thermometry probes (Luxtron 3100 Fluoroptic Thermometer, LumaSense Technologies, Santa Clara, CA, USA). The probes sampled the temperature at the probe location with a temporal resolution of 2 seconds. All images were reconstructed from the raw k-space data with custom written software in the MATLAB environment (MathWorks, Natick, MA, USA). For our protocols (with echo times around 2.5 ms) the $TmDOTMA^-$ phase wraps occur every 1.8 °C, therefore phase unwrapping had to be performed on the reconstructed phase images. Temperature maps were calculated from the phase images using the formula in Eq. [1].

Three temperature imaging experiments were conducted. Firstly, a temperature imaging calibration and validation experiment was performed on a test sample. Then, two experiments were conducted with the anthropomorphic phantom: 1) a birdcage coil heating experiment to measure the heating pattern expected from a typical human experiment and 2) a local RF coil heating experiment, in which heat was deposited with a local RF loop coil to generate focal heating and a steep spatial temperature gradient. A summary of all the imaging parameters used in the temperature mapping can be found in Table 2. In addition, we acquired B_1^+ field maps using the method of Fautz et al. (31).

Temperature imaging calibration

To confirm the coefficient *c* for $TmDOTMA^-$ and to calibrate our temperature imaging protocol, a cooling experiment was performed using a small sample of water containing 4 mM $TmDOTMA^-$ in a 30 mm 4-turn solenoid coil (for transmit and receive). RF heating was applied using a Turbo Spin-Echo sequence, chosen for its train of 180° refocusing pulses. During the cooling, 3D GRE phase images were continuously acquired for 60 min using the parameter values in Table 2. The final phase image (i.e., the data from the scan at

the lowest temperature) was used as a baseline. The phase difference was unwrapped over time for each voxel. Temporal phase unwrapping was feasible in this experiment since our acquisition was fast enough to prevent phase shifts larger than 2π between consecutively acquired phase images.

The phase difference data was averaged over a volume-of-interest of 4.8 cm^3 centered around the fiber optic probe tip, which could be visualized on a high-resolution water image of the sample. A linear least-squares fit was used to fit the temperature coefficient *c* for $TmDOTMA^-$ based on the temperature recorded by the fiber-optic probe and the measured phase shifts. As a validation, the same experiment was repeated and the MR temperature measurements were compared to the fiber optic probe data.

RF heating experiments with the anthropomorphic phantom

For imaging experiments with the human head phantom, a custom-built 32-channel phased-array helmet coil (32) was used for receive and a custom-built detunable band-pass birdcage coil was used for transmit. Heating was monitored and measured using two fiber optic probes inserted into the brain compartment of the phantom. Each probe's position was located on a high-resolution water image, and a region of four voxels enclosing 0.5 cm^3 was chosen close to the location of the fiber optic probe tips. The fiber optic probe data was compared to the average temperature measured within this ROI from the temperature imaging data.

Birdcage coil heating experiment—Using the birdcage volume coil for excitation, a 3D GRE sequence was used both for heating and for the acquisition of temperature maps. The imaging parameters are listed in Table 2. Phase unwrapping over time was performed for each voxel, as done in the calibration experiment. The first phase image acquired (i.e. the scan at the lowest temperature) was used as the baseline phase image. The temperature maps were repeated 17 times over a total of 27 minutes.

Local RF coil heating experiment—An RF loop coil with inner diameter 7 cm was used as a local RF heat deposition source. The coil was placed at the side (on the left temple) of the phantom as indicated in Fig. 4. A multi-echo GRE sequence was used for imaging. A baseline phase image was acquired before the application of the local RF. Then 50 W of continuous wave RF power was applied to the input coax for 16 minutes. The loop coil was tuned to 305 MHz—slightly above the resonance of the imaging coils—and therefore could be left in place during the imaging. The second phase image was taken 10 minutes after the application of the RF energy. Due to the short T_2^* value of $TmDOTMA^-$ only the first echo was used to generate the temperature maps (see Fig. 2b). The combined magnitude images of all four echoes were used to generate a mask. Since in this experiment temporal phase unwrapping is not possible, spatial phase unwrapping was performed on each of the reconstructed phase images using the “prelude” application of the FSL software package (http://www.fmrib.ox.ac.uk/fsl/).

Results

The result of the phantom construction was assessed using both CT to image the plastic compartment and MRI to inspect the agar gels, as shown in Fig. 3. The measured B_1^+ pattern (see Fig. 3d) of the phantom shows central brightening and the characteristic bilateral signal drop-off in the temporal lobes, which matches the typical pattern observed in vivo at 7 T (5).

The results of the temperature imaging calibration are displayed in Fig. 4. The temperature constant, *c*, of $TmDOTMA^-$ was determined to be 0.62 ppm/°C, which is in good agreement with literature values (23,33). In the second validation experiment with this configuration, we used the previously measured temperature coefficient and determined a mean absolute error of 0.04 °C compared to the fiber optic probes (see Fig. 4a).

In the birdcage coil heating experiment, where the anthropomorphic phantom was heated by the 3D GRE imaging sequence itself, the temperature was seen to rise up to almost 2 °C in the top part of the brain compartment after 30 minutes of continuous imaging at nearly 100% of the permitted SAR. Most regions of the phantom however experienced temperature increases lower than 1.5 °C. An example temperature map and an example slice of a high-resolution water scout image are shown in Fig. 5. The temperature curves over time for two locations within the phantom can be seen in Fig. 5, where the temperature can be seen to increase approximately linearly with time. A mean absolute error of 0.08 °C and 0.04 °C between the temperature measurement and the fiber optic probe measurement was determined for probe 1 and 2, respectively.

In the local RF coil heating experiment a clear temperature increase was seen at the location of the RF loop coil (see temperature map in Fig. 6). The maximum temperature increase detected was 7.5 °C in the area located directly under the loop coil.

Discussion

This study was aimed at addressing one of the shortfalls of standard MRI phantoms by creating an anthropomorphic phantom with realistic shape and dielectric properties distribution. Such a phantom can be used to evaluate the energy deposition of RF pulses. The shape of the phantom is relevant because the paths of the induced electrical currents strongly depend on the geometry of the high conductivity tissues, which can have a complicated geometry in the human body. This non-uniformity of the electric properties therefore dominates the shape of the electric fields generated in the phantom and hence the SAR and temperature pattern. Additionally, constructive or destructive interferences of the fields created by the current-carrying elements in the coil are strongly affected by the geometric distribution of conductivity, and contribute to the dependence of energy deposition on the shape of the phantom. For this reason a uniform phantom geometry cannot predict the focal heating, which can occur in human subjects.

Thus both the dielectric constant value and the tissue compartment shape must correctly mimic the human head. In contrast, most MRI phantoms currently being utilized are geometrically simple, homogeneous objects (e.g., (34,35)) that do not accurately mimic the

dielectric properties of human tissue. Other important considerations which favor an anthropomorphic phantom include the need to load the transmit and receive arrays in a similar fashion to the head. This requires a realistic human shape for tightly fitting array coils whose form follows the body contour. Finally, the anthropomorphic phantom is useful for sequence testing and artifact debugging, since many artifacts (such as aliasing) are influenced by the object shape. A range of anthropomorphic phantoms have been developed over the years, with several commercially available. Most of these are intended for imaging calibration purposes (matching relaxation/susceptibility properties instead of dielectric properties), for example head phantoms by Shmueli et al. (36) which includes air cavities to mimic magnetic susceptibility artifacts, or by Kuss et al. (37) which utilized a real skull filled with Agar gel whose goal was to realistically test cortical electrode placement measurements. Freed et al. (38) developed an anthropomorphic phantom with anatomical structure to evaluate quantitative breast protocols. There are also a range of anthropomorphic phantoms for x-ray dosimetry and image calibration (such as (39)) and for other imaging modalities, for example for microwave imaging (40).

Other efforts have focused on realistic dielectric properties. This (work) includes techniques for developing the phantom materials (26,41). The CHEMA phantom combines realistic dielectric properties with an anthropomorphic shape but compared to the phantom presented in this work it consists of only a single compartment (42). The Specific Anthropomorphic Mannequin (SAM) phantom is widely used for SAR evaluation in the telecommunication industry (IEEE SCC-34). Similar to the CHEMA phantom it is a head/neck container filled with a homogeneous fluid having the average electrical properties of head tissue at the test frequency.

Phantom design and fabrication

The fabrication of a phantom with an accurate geometry presents many technical challenges, especially when containing multiple tissue compartments. This work (together with other recent work, such as for example a ventricle phantom for MRI (43)) shows that 3D printing is a promising technology for a new generation of more realistic MRI phantoms.

While the constructed phantom mimics the basic brain compartments and dielectric constants, it lacks several temperature regulation methods of the living brain. Also, the plastic shell layer provides a thermally insulating layer and therefore the phantom cools very slowly. Thus the temperature maps from the phantom likely represent a conservative estimate of those present in vivo. However, this might be appropriate as a “worst case” estimate for populations that include subjects/patients with compromised blood flow or compromised thermal regulation.

We have demonstrated the utility of this realistic head phantom for temperature imaging, however there are potential design and construction improvements that may be considered for future iterations. For example, while the bone and air structure is modeled quite accurately by the 3D printed plastic (bone, air and plastic have low conductivity and low dielectric constant) the plastic is not an optimal model for fat (which has a low dielectric constant but a higher conductivity), and other tissue types in the low dielectric compartment. Additionally, even if the plastic could fully mimic the electrical properties, these tissues

have density and thermal properties, which differ from the PC-ABS plastic. For this reason some of the plastic could be replaced with materials modeling some of the tissues included in the low dielectric compartment more accurately. There are limitations to this since the plastic also provides the mechanical support for the gel phantom.

Ideally, adjacent tissues would be represented by gels that are directly touching without any plastic container (similar to what was done in (37)), since any artificial boundary will affect the electrical and thermal coupling between the adjacent tissues. And it might be useful to include more tissue classes, for example the cerebrospinal fluid, which has higher conductivity. However this expanded design would increase the geometric complexity of the internal compartments of the phantom, and would create new challenges to fill these compartments with the appropriate tissue-mimicking gels. The match to the electromagnetic fields generated in vivo could also be improved by including the neck and shoulders into the phantom.

Ideally in addition to the electrical properties the thermal properties (e.g., the heat conductivity) should also be matched to the real tissue types. While we did not measure the thermal properties of our phantom materials Ito et al. (26) reported that their phantom materials, which are similar to the ones used in this project, have thermal properties close to the ones of real human tissue.

We tried to match electrical properties but did not attempt to match MR relaxation properties. This could be achieved for example by additionally adding appropriate amounts of R_1, R_2, and R_2* contrast agents to achieve the desired T_1, T_2 and T_2* values respectively.

Temperature imaging

The temperature imaging performed provides sufficient temperature contrast-to-noise ratio to yield good agreement with the published chemical shift coefficient *c* and it also matches the fiber optic probe measurements with very high accuracy.

Using temperature imaging to evaluate the power deposition and heating caused by RF pulses imposes many strict requirements on the imaging protocol, several of which pose competing constraints which must be carefully balanced. A major constraint placed on the temperature imaging protocol is that the acquisition must be extremely rapid otherwise the temperature pattern will change over the imaging time due to diffusion of heat, which could lead to a loss of valuable information if, e.g., temperature hotspots would disappear as a result. Furthermore the imaging protocol itself should deposit minimal power, because it will not be possible to separate the heating caused by the imaging protocol from the heating deposited by the transmit pulses under evaluation. Solutions to these challenges must be balanced with the very low concentration of $TmDOTMA^-$ protons, which reduces the image SNR relative to water, the relatively short relaxation times of $TmDOTMA^-$ (at 9.4 T: T_1 = 5.3 ms and T_2 = 4.1 ms (23)) and the restricted gradient performance of whole-body human scanners compared to previous $TmDOTMA^-$ studies conducted on small-bore scanners.

We found that the concentration of $TmDOTMA^-$ we used (2 mM) was probably the minimum acceptable level required to perform temperature imaging with this phantom, and

that thermometry using the ^{1}H signal of water would most likely be nearly equally sensitive for this situation. Using thermometry on water would facilitate the MR acquisition and analysis of the temperature maps and would make the phantom production less expensive. However, increasing the concentration of $TmDOTMA^{-}$ is a straightforward way to directly increase the sensitivity of the measurement and to surpass the sensitivity of water thermometry. If the high monetary cost of $TmDOTMA^{-}$ were not prohibitive the concentration should be significantly increased, which would improve the sensitivity of the temperature measurement allowing shorter scans and/or reduced flip angle imaging thus reducing the SAR of the measurement protocol itself. The many tradeoffs between water and $TmDOTMA^{-}$ must be carefully evaluated against the temperature contrast-to-noise ratio afforded by each.

Acquiring at multiple TEs is an efficient strategy for generating frequency maps (similar to the procedure used for standard B_0 mapping) and eliminates the need for the phase unwrapping if the ΔTE is short enough. However due to the short T_2^* of the $TmDOTMA^{-}$ and limited gradient strength of human scanners (necessitating $\Delta TE = 1.67$ ms), it was not possible to acquire more than two echoes with a reasonable SNR (see Fig. 2). This ΔTE was not short enough to prevent phase wraps. This issue could be addressed by using multiple excitations and acquiring images with a narrow range of TE values; however this would be at the expense of increased acquisition time and increased heat deposition by the temperature imaging sequence.

Use of the phantom in MR safety

Phantom measurements make up only one part of a comprehensive safety evaluation for an RF transmitter geometry. Other methods include electromagnetic simulations in realistic body models, thermal simulations, thermal measurements in simple phantom geometries and thermal measurements in animal models. Phantom experiments have the advantage of convenience and robustness and that temperature sensitive compounds, such as $TmDOTMA^{-}$, can be added.

Currently temperature hotspots are usually predicted using electromagnetic and temperature simulations in a human body model. This is a complicated two-step process involving an electromagnetic simulation to calculate the electric field distribution followed by solving the heat equation to calculate the temperature increase. This phantom could be a useful tool to evaluate the final temperature simulation results since the simulations could use the same CAD model that was the basis for the phantom fabrication. It will hence be possible to simulate heating with an extremely accurate geometric representation of the constructed phantom even with its complex internal structure, enabling direct voxel-by-voxel comparison of simulated and measured 3D temperature maps.

Conclusion

We have demonstrated that the construction of an anatomically and electrically realistic phantom of the human head is feasible and useful for 3D temperature mapping. We achieved a temperature accuracy better than 0.1°C in a phantom with field patterns mimicking those in the human head. The anthropomorphic head phantom presented in this work provides a

tool suitable for routine testing of coils and RF pulses. It will be useful for the assessment of the heating caused by pTx pulses and for the validation of electromagnetic and temperature simulations of the human head in pTx arrays.

Acknowledgments

The authors would like to thank Drs. Daniel Schuehle and Peter Caravan for the synthesis of the $TmDOTMA^{-}$. The authors also thank Drs. Boris Keil and Thomas Witzel for their help with conducting the temperature imaging experiments, Dr. Matt Rosen for lending equipment for the experiments, and Dr. Giorgio Bonmassar for providing the hand-labeled anatomical data. This work was supported by NIH NCRR grant P41-RR14075 and NIBIB grants R01-EB006847 and K01-EB011498 and the EPFL Wish foundation.

References

1. Davis PL, Shang C, Talagala L, Pasculle AW. Magnetic resonance imaging can cause focal heating in a nonuniform phantom. IEEE Trans Biomed Eng. 1993; 40:1324–1327. doi:10.1109/10.250588. [PubMed: 8125508]
2. Collins CM, Li S, Smith MB. SAR and B1 field distributions in a heterogeneous human head model within a birdcage coil. Magn. Reson. Med. 1998; 40:847–856. [PubMed: 9840829]
3. Zhu Y. Parallel excitation with an array of transmit coils. Magn. Reson. Med. 2004; 51:775–784. [PubMed: 15065251]
4. Katscher U, Börnert P, Leussler C, van den Brink JS. Transmit SENSE. Magn. Reson. Med. 2003; 49:144–150. [PubMed: 12509830]
5. Collins CM, Liu W, Schreiber W, Yang QX, Smith MB. Central brightening due to constructive interference with, without, and despite dielectric resonance. J Magn Reson Imaging. 2005; 21:192–196. [PubMed: 15666397]
6. van de Moortele P-F, Akgun C, Adriany G, Moeller S, Ritter J, Collins CM, Smith MB, Vaughan JT, Ugurbil K. B(1) destructive interferences and spatial phase patterns at 7 T with a head transceiver array coil. Magn. Reson. Med. 2005; 54:1503–1518. [PubMed: 16270333]
7. Vaughan JT, Snyder CJ, DelaBarre LJ, Bolan PJ, Tian J, Bolinger L, Adriany G, Andersen P, Strupp J, Ugurbil K. Whole-body imaging at 7T: Preliminary results. Magn. Reson. Med. 2009; 61:244–248. [PubMed: 19097214]
8. Zelinski AC, Angelone LM, Goyal VK, Bonmassar G, Adalsteinsson E, Wald LL. Specific absorption rate studies of the parallel transmission of inner-volume excitations at 7T. J Magn Reson Imaging. 2008; 28:1005–1018. [PubMed: 18821601]
9. Guérin B, Gebhardt M, Cauley S, Adalsteinsson E, Wald LL. Local specific absorption rate (SAR), global SAR, transmitter power, and excitation accuracy trade-offs in low flip-angle parallel transmit pulse design. Magn. Reson. Med. 2013 doi: 10.1002/mrm.24800.
10. Voigt T, Homann H, Katscher U, Doessel O. Patient-individual local SAR determination: in vivo measurements and numerical validation. Magn. Reson. Med. 2012; 68:1117–1126. [PubMed: 22213053]
11. Collins CM, Liu W, Wang J, Gruetter R, Vaughan JT, Ugurbil K, Smith MB. Temperature and SAR calculations for a human head within volume and surface coils at 64 and 300 MHz. J Magn Reson Imaging. 2004; 19:650–656. [PubMed: 15112317]
12. Massire A, Cloos MA, Luong M, Amadon A, Vignaud A, Wiggins CJ, Boulant N. Thermal simulations in the human head for high field MRI using parallel transmission. J Magn Reson Imaging. 2012; 35:1312–1321. [PubMed: 22241685]
13. Oh S, Ryu Y-C, Carluccio G, Sica CT, Collins CM. Measurement of SAR-induced temperature increase in a phantom and in vivo with comparison to numerical simulation. Magn. Reson. Med. 2013 doi: 10.1002/mrm.24820.
14. Oh S, Webb AG, Neuberger T, Park B, Collins CM. Experimental and numerical assessment of MRI-induced temperature change and SAR distributions in phantoms and in vivo. Magn. Reson. Med. 2010; 63:218–223. doi: 10.1002/mrm.22174. [PubMed: 19785018]

15. Lepetit-Coiffé M, Quesson B, Seror O, Dumont E, Le Bail B, Moonen CTW, Trillaud H. Real-time monitoring of radiofrequency ablation of rabbit liver by respiratory-gated quantitative temperature MRI. J Magn Reson Imaging. 2006; 24:152–159. doi: 10.1002/jmri.20605. [PubMed: 16767739]
16. Rieke V, Kinsey AM, Ross AB, Nau WH, Diederich CJ, Sommer G, Pauly KB. Referenceless MR thermometry for monitoring thermal ablation in the prostate. IEEE Trans Med Imaging. 2007; 26:813–821. doi: 10.1109/TMI.2007.892647. [PubMed: 17679332]
17. Salomir R, Vimeux FC, de Zwart JA, Grenier N, Moonen CT. Hyperthermia by MR-guided focused ultrasound: accurate temperature control based on fast MRI and a physical model of local energy deposition and heat conduction. Magn. Reson. Med. 2000; 43:342–347. [PubMed: 10725875]
18. Gellermann J. Noninvasive Magnetic Resonance Thermography of Recurrent Rectal Carcinoma in a 1.5 Tesla Hybrid System. Cancer Research. 2005; 65:5872–5880. doi: 10.1158/0008-5472.CAN-04-3952. [PubMed: 15994965]
19. Piaskowski, MJ. Threshold determination of tissue damage caused by high frequency fields in MRI in swine model [dissertation]. [Internet]. FU Berlin; Berlin, DE: 2012. Available from http://www.diss.fu-berlin.de [2013 Nov 25]
20. Shrivastava D, Hanson T, Kulesa J, Tian J, Adriany G, Vaughan JT. Radiofrequency heating in porcine models with a “large” 32 cm internal diameter, 7 T (296 MHz) head coil. Magn. Reson. Med. [Internet]. 2011; 66:255–263.
21. Shrivastava D, Hanson T, Kulesa J, DelaBarre L, Iaizzo P, Vaughan JT. Radio frequency heating at 9.4T (400.2 MHz): In vivo thermoregulatory temperature response in swine. Magn. Reson. Med. 2009; 62:888–895. [PubMed: 19572392]
22. Shellock FG. Radiofrequency Energy-Induced Heating During MR Procedures: A Review. J Magn Reson Imaging. 2000; 12:30–36. [PubMed: 10931562]
23. Hekmatyar SK, Hopewell P, Pakin SK, Babsky A, Bansal N. Noninvasive MR thermometry using paramagnetic lanthanide complexes of 1,4,7,10-tetraazacyclodoecane- alpha,alpha’,alpha”,alpha’ “-”tetramethyl-1,4,7,10-tetraacetic acid (DOTMA4-). Magn. Reson. Med. 2005; 53:294–303. [PubMed: 15678553]
24. Makris N, Angelone L, Tulloch S, Sorg S, Kaiser J, Kennedy D, Bonmassar G. MRI-based anatomical model of the human head for specific absorption rate mapping. Med. Biol. Eng. Comput. 2008; 46:1239–1251. [PubMed: 18985401]
25. Park SM, Nyenhuis JA, Smith CD, et al. Gelled versus nongelled phantom material for measurement of MRI-induced temperature increases with bioimplants. IEEE Transactions on Magnetics. 2003; 39:3367–3371.
26. Ito K, Furuya K, Okano Y, Hamada L. Development and characteristics of a biological tissue equivalent phantom for microwaves. Electron. Comm. Jpn. Pt. 1. 2001; 84:1126–1135.
27. Gabriel S, Lau RW, Gabriel C. The dielectric properties of biological tissues: III. Parametric models for the dielectric spectrum of tissues. Phys. Med. Biol. 1999; 41:2271–2293. [PubMed: 8938026]
28. Miller AK, Alston RL, Corsellis JA. Variation with age in the volumes of grey and white matter in the cerebral hemispheres of man: measurements with an image analyser. Neuropathol Appl Neurobiol. 1980; 6:119–132. [PubMed: 7374914]
29. Ishihara Y, Calderon A, Watanabe H, Okamoto K, Suzuki Y, Kuroda K, Suzuki Y. A precise and fast temperature mapping using water proton chemical shift. Magn. Reson. Med. 1995; 34:814–823. [PubMed: 8598808]
30. Shapiro EM, Borthakur A, Shapiro MJ, Reddy R, Leigh JS. Fast MRI of RF heating via phase difference mapping. Magn. Reson. Med. 2002; 47:492–498. [PubMed: 11870836]
31. Fautz HP, Vogel M, Gross P, Kerr A, Zhu Y. B1 mapping of coil arrays for parallel transmission. Proc. Intl. Soc. Mag. Reson. Med. 2008; 16:1247.
32. Keil B, Triantafyllou C, Hamm M. Design optimization of a 32-channel head coil at 7 T. Proc. Intl. Soc. Mag. Reson. Med. 2010:18.
33. James JR, Gao Y, Miller MA, Babsky A, Bansal N. Absolute temperature MR imaging with thulium 1,4,7,10-tetraazacyclododecane-1,4,7,10-tetramethyl-1,4,7,10-tetraacetic acid (TmDOTMA —). Magn. Reson. Med. 2009; 62:550–556. [PubMed: 19526494]

34. Kawamura T, Saito K, Kikuchi S, Takahashi M, Ito K. Specific Absorption Rate Measurement of Birdcage Coil for 3.0-T Magnetic Resonance Imaging System Employing Thermographic Method. IEEE Trans. Microwave Theory Techn. 2009; 57:2508–2514.
35. Xin X, Han J, Wang D, Feng Y, Feng Q, Chen W. Development of a calibration phantom set for MRI temperature imaging system quality assurance. Acad Radiol. 2012:740–745. [PubMed: 22459644]
36. Shmueli K, Thomas DL, Ordidge RJ. Design, construction and evaluation of an anthropomorphic head phantom with realistic susceptibility artifacts. J Magn Reson Imaging. 2007; 26:202–207. [PubMed: 17659546]
37. Kuß J, Wagner S, Meyer T, Kirsch M, Werner A, Schackert G, Kummer von R, Morgenstern U. A head phantom prototype to verify subdural electrode localization tools in epilepsy surgery. Neuroimage. 2011; 54:256–262.
38. Freed M, de Zwart JA, Loud JT, Khouli El RH, Myers KJ, Greene MH, Duyn JH, Badano A. An anthropomorphic phantom for quantitative evaluation of breast MRI. Med Phys. 2011; 38:743–753. [PubMed: 21452712]
39. Winslow JF, Hyer DE, Fisher RF, Tien CJ, Hintenlang DE. Construction of anthropomorphic phantoms for use in dosimetry studies. J Appl Clin Med Phys. 2009; 10:195–204.
40. Mashal A, Gao F, Hagness SC. Heterogeneous Anthropomorphic Phantoms with Realistic Dielectric Properties for Microwave Breast Imaging Experiments. Microw Opt Technol Lett. 2011; 53:1896–1902. [PubMed: 21866208]
41. Tofts PS, Barker GJ, Dean TL, Gallagher H, Gregory AP, Clarke RN. A low dielectric constant customized phantom design to measure RF coil nonuniformity. Magn Reson Med. 1997; 15:69–75.
42. Angelone LM, Vasios CE, Wiggins G, Purdon PL, Bonmassar G. On the effect of resistive EEG electrodes and leads during 7 T MRI: simulation and temperature measurement studies. Magn Reson Med. 2006; 24:801–812.
43. Khan AF, Drozd JJ, Moreland RK, Ta RM. A novel MRI compatible brain ventricle phantom for validation of segmentation and volumetry methods. J Magn Reson Imaging. 2012; 36:476–482. [PubMed: 22396226]

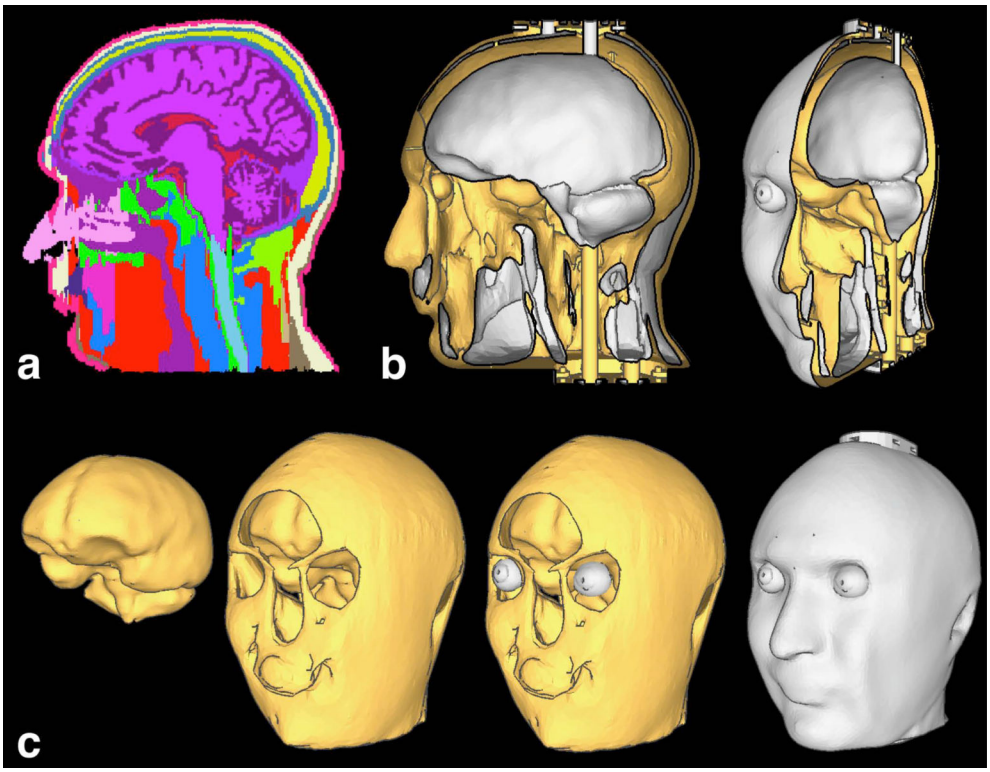

FIG. 1. Phantom design

(a) The 37 tissue type model generated from 1 mm isotropic MR image volumes of a human head. (b) Sagittal cut through CAD model, shown in lateral and oblique views. White corresponds to outside surfaces or surfaces facing the cavities, whereas yellow surfaces are facing regions printed in plastic. (c) From left to right: surface meshes for the brain, muscle, the eyes and the plastic compartment.

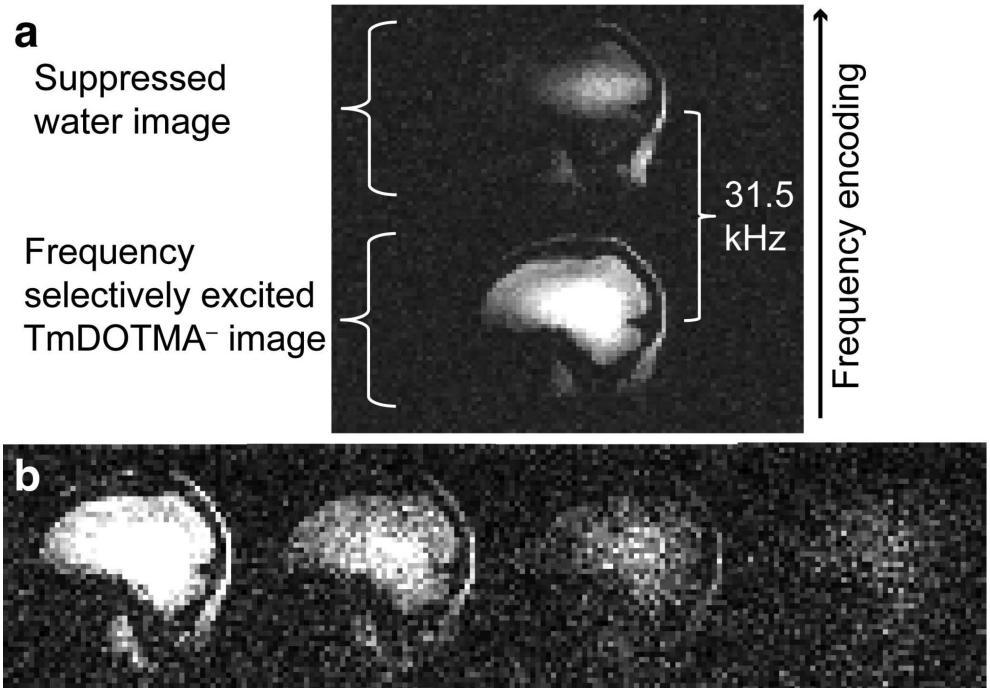

FIG. 2. TmDOTMA$^-$ imaging

(a) Water and TmDOTMA$^-$ images separated by 31.5 kHz in frequency encoding direction. (b) Four echoes acquired with multi-echo GRE, TE_1 = 2.5 ms, ΔTE = 1.67 ms. The measured signal decay is consistent with a T_2* of approximately 4 ms.

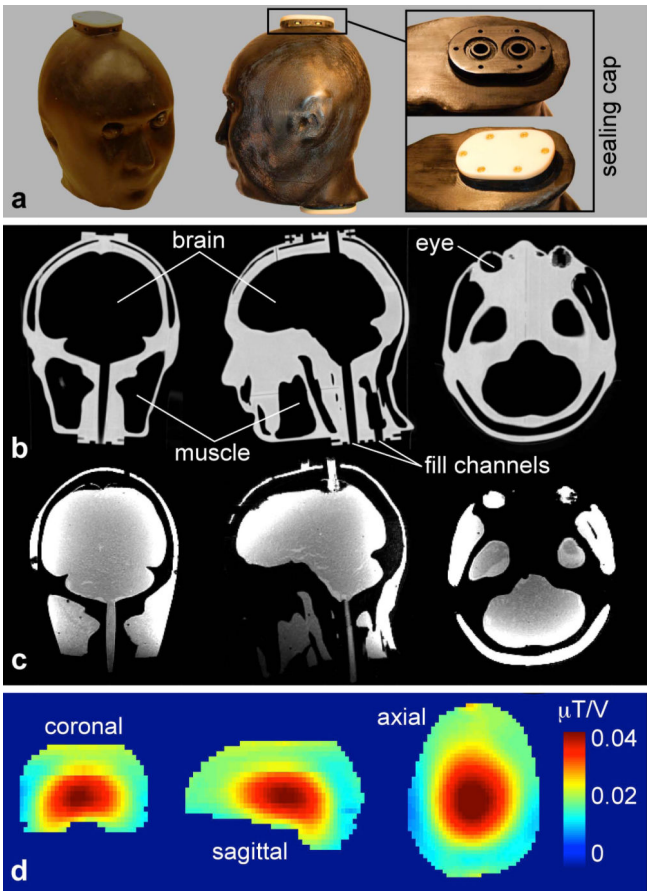

FIG. 3. Constructed phantom

(a) Photographs of the completed phantom. From left to right: Front view, side view and details of the mechanical sealing: o-ring indentations surrounding filling channels and small holes for screws (top) and screwed on sealing cap (bottom) (b) CT scan of the empty phantom. (c) MRI of completed phantom filled with gel. (d) B_1^+ map (magnitude) of the gel-filled phantom at 7 T.

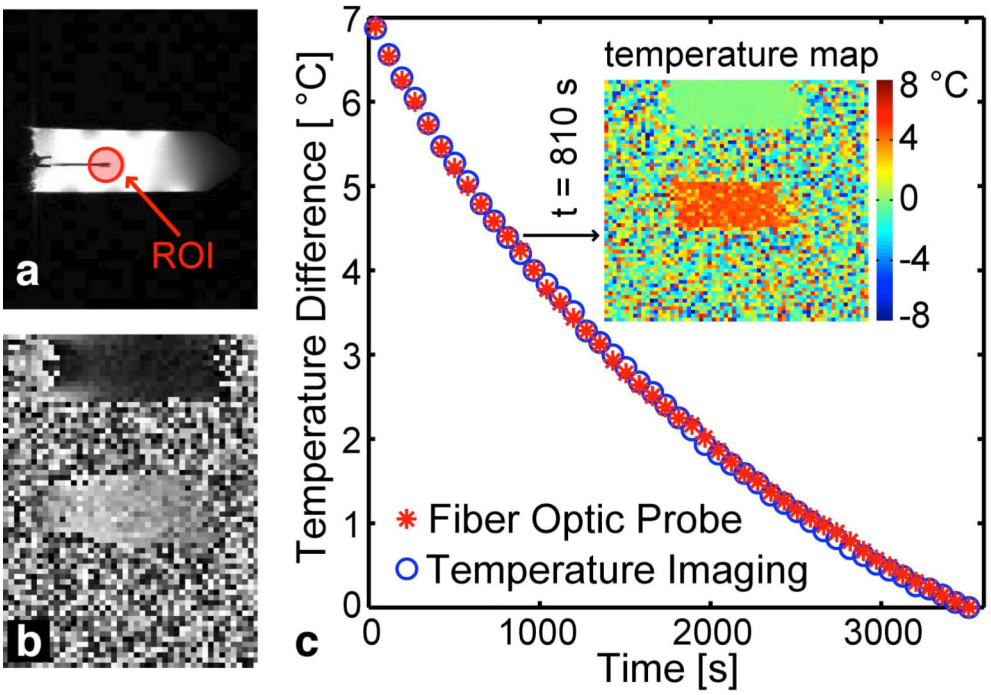

FIG. 4. Temperature imaging calibration

(a) Water image showing test tube and fiber optic probe inserted into the tube. The red circle shows approximate position of ROI around the probe tip. (b) Phase image acquired at the $TmDOTMA^{-}$ resonance frequency. (c) Cooling curve measured simultaneously with fiber optic probe (red asterisks) and temperature imaging (blue circles) demonstrating accurate calibration of temperature imaging. *Insert:* Example temperature map at t = 810 s after the beginning of the experiment.

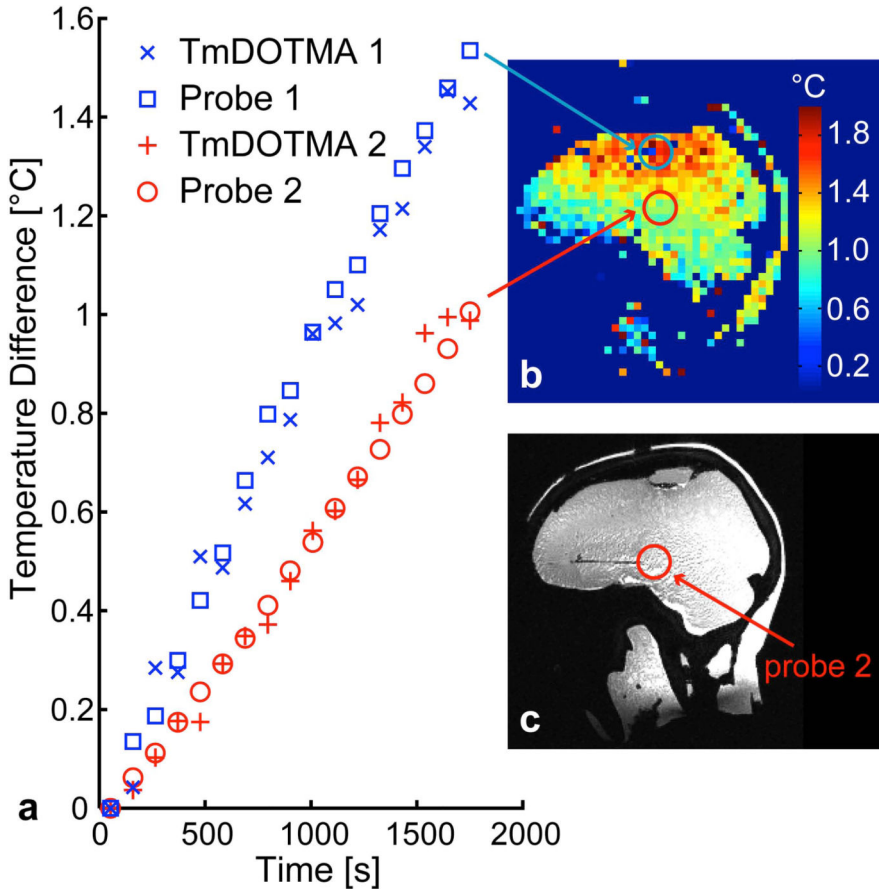

FIG. 5. Birdcage coil heating experiment

(a) Temperature change over time for two locations in the phantom experiencing different amounts of heating. The temperature curves measured by the fiber optic probes and the temperature calculated from the temperature imaging using an ROI of 4 voxels (0.5 cm^3) around the probe tip (blue = fiber optic probe 1, red = fiber optic probe 2) are displayed. (b) Example sagittal slice of temperature map for t = 30 min (after onset of imaging/heating), approximate locations of ROIs at probe tips marked with circles. Note the red circle marks the location of the one probe tip located within this slice—the blue circle marks the point within the slice nearest to the second probe tip. (c) Water image used to locate probe tip, with the approximate location of one fiber optic probe marked with red circle.

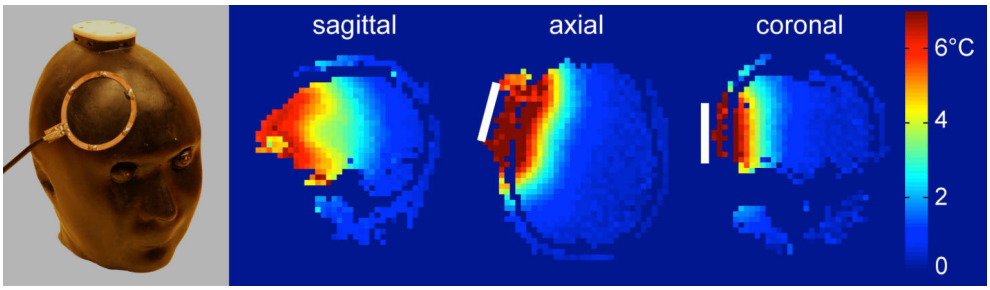

FIG. 6. Local RF coil heating experiment

(a) Photograph of the phantom with the RF loop coil used for the local heating experiment. (b) Relative temperature maps shown in sagittal, axial and coronal views at t = 10 min after RF heating. The white bar indicates the approximate position of the RF loop coil

Table 1

Phantom materials

Compositions used for the brain, muscle and eye tissue phantom materials.

Weight Percent	Brain	Muscle	Eyes
Agar	2	2	2
Salt (NaCl)	0.4	0.5	0.8
Sodium Azide (NaN_3)	0.05	0.05	0.05
Polyethylene Powder	15	10	5
Deionized H_20	100	100	100

Table 2

Imaging parameters

Parameters used for the three temperature mapping experiments.

Imaging parameters	Temperature imaging calibration	Birdcage coil heating	Local RF coil heating
Sequence	3D GRE	3D GRE	3D multi-echo GRE
TR [ms]/ TE_1,TE_2...[ms]	10 / 3	11/ 4.2	11/ 2.5, 4.17, 5.84, 7.51
Resolution [mm]	2×2×2	5×5×5	5×5×5
Encoding matrix	64×64×24	48×48×40	48×48×40
Bandwidth [kHz]	75.8	76.9	76.9
Number of averages	5	5	10
Total acquisition time [s]	75	106	211